Latest draft 4/11/2018
Preprint typeset using LaTeX style emulateapj v. 01/23/15

PROPERTIES OF THE HOT CIRCUMGALACTIC MEDIUM OF EARLY TYPE GALAXY HOSTS WITH POWERFUL RADIO SOURCES

Frisbie, Rachel L.S., Donahue, Megan, Voit, G. Mark
Physics & Astronomy Department Michigan State University

Li, Yuan
Kavli New York

Sun, Ming
University of Alabama

Connor, Thomas
Carnegie Observatories

Werner, Norbert
Eotvos University, Hungary
Latest draft 4/11/2018

ABSTRACT

We present an archival analysis of Chandra X-ray data for nearby early type galaxies with powerful radio sources. Previously, in a similar analysis of eight nearby X-ray and optically-bright elliptical galaxies, Werner et al., found that NGC4261 exhibited unusually low central entropy for the sample as well as a t_{cool}/t_{ff} below the expected threshold of 10, indicating that rapid precipitation is providing cool gas, condensed from the hot circumgalactic medium (CGM), as fuel for accretion in the central region. NGC4261 also hosts the most powerful radio source in the Werner sample. Our sample is comprised of twelve nearby early type galaxies with powerful radio sources, that is, galaxies with similar properties to NGC4261; to determine if NGC4261 is a unique system or perhaps represents a transitional phase during which powerful feedback from a central active galactic nucleus (AGN) is fueled by feedback in the central kpc. We present entropy profiles as well as profiles of the ratio between the cooling time and free-fall time of the galaxy. We find that at least one of these sources, IC4296, exhibits similar properties to NGC4261 and therefore NGC4261 is not unique but may be unusual. Hydrodynamic simulations of AGN feedback fueled by CGM precipitation at the galaxy scale predict CGM halo gradients similar to our measurements for these galaxies.

Keywords: X-rays: galaxies-galaxies: cooling flows-ISM-galaxies: active

1. INTRODUCTION

We can use the insights from galaxy clusters to help decode galaxies with central black holes and gas (Voit & Donahue 2015), and nearby galaxies provide the increased spatial resolution we need to observe the gas close to the black hole. Because the gravitational potential depths are different between galaxies and galaxy clusters, supernova explosions and galactic winds are energetically a more important piece of the story for galaxies than galaxy clusters. Because they are less massive than galaxy clusters, the particles are less bound to each other which means that the hot gas surrounding an early-type galaxy may be more affected by feedback processes than the gas surrounding a brightest cluster galaxy (BCG) (Voit et al. 2015b), the brightest and most massive galaxy in a galaxy cluster.

Evidence suggests that black holes somehow suppress the star formation in massive galaxies (McNamara & Nulsen (2007), McNamara & Nulsen (2012)), but how the accretion of the black hole is affected by the surrounding hot gas is less clear. Precipitation-driven feedback models explain the coupling between the black hole and hot gas as a relationship between the gas entropy, which is regulated by energy injected by the black hole, and the rate at which that gas cools and provides fuel for the black hole's activity.

Individually, the temperature and density of the X-ray gas do not reveal the thermal history of a galaxy or galaxy cluster because one parameter can vary while the other remains constant. However, if we combine these two X-ray observables and use them to rewrite the classical definition of entropy ($K \propto P\rho^{-5/3}$, where P is the gas pressure and ρ is the gas density), we can now define our gas entropy $K = T_X n_e^{-2/3}$, where T_X is the temperature of the X-ray gas and n_e is the electron density of the X-ray gas. Only gains and losses of energy in the gas can change the entropy, so we can trace the thermal history of the gas in the galaxy or galaxy cluster.

Numerical simulations show that cool clouds can precipitate out of a galaxy's hot-gas atmosphere via thermal instability even if it is in a state of global thermal balance, with heating approximately equal to cooling (Mc-

Court et al. (2012), Sharma et al. (2012), Gaspari et al. (2012), see also Pizzolato & Soker (2005)). The critical criterion for precipitation depends on the ratio between the time t_{cool} required for gas at temperature T to radiate $3kT/2$ per particle and the free-fall time $t_{ff} = (2r/g)^{1/2}$ required for a dense cool cloud to fall from a radius r at the local gravitational acceleration g. In both observations and in simulations (McCourt et al. (2012), Sharma et al. (2012), Gaspari et al. (2012), Li & Bryan (2014a)), when the average t_{cool}/t_{ff} ratio is less than 10, cooling is fast enough for some of the hot gas to condense into cold clouds and precipitate out of the hot medium. Precipitation itself plays an essential role in maintaining the required state of global thermal balance because it provides fuel for accretion. Recent numerical simulations of this feedback loop have been very encouraging because they show that chaotic cold accretion of precipitating clouds can produce a black-hole fueling rate two orders of magnitude greater than the Bondi rate and can therefore generate a feedback response that brings the system into approximate balance at $t_{cool}/t_{ff} \approx 10$ (Gaspari et al. (2013),Gaspari et al. (2015); Li & Bryan (2014a),Li & Bryan (2014b), see also Pizzolato & Soker (2010)).

Voit et al. (2015a) showed that the t_{cool}/t_{ff} ratio holds for early type galaxies. They can be broken into two categories: single-phase galaxies and multi-phase galaxies. Multi-phase galaxies have extended Hα present outside their cores (central ∼kpc), and single-phase galaxies have no evidence for extended Hα outside of their cores. X-ray observations of giant ellipticals by Werner et al. 2012, 2014 showed that they have similar entropies ($K \sim 2$keVcm^2) at $\sim$ 1kpc, but are distinctly bimodal from 1-10 kpc. Single phase galaxies scale with r and multi-phase galaxies scale with $r^{2/3}$ for this range, and they both exhibit a core excess inside $\sim$ 1kpc.

However, X-ray observations of NGC4261 from Werner et al. (2012) revealed an entropy profile that followed a single power law into the central $\sim$ 0.5 kpc and $t_{cool}/t_{ff} < 10$ in the core. NGC4261 also has radio luminosity 2 orders of magnitude greater than the rest of the Werner et al. (2012) sample and a jet power of 10^{44} erg s^{-1}, too great to be due to Bondi accretion alone. Assuming a central black hole mass of $M_{BH} = 5 \times 10^8 M_\odot$ (Gaspari et al. (2013)) and $K \approx 0.8$ keV cm^2 in the central bin, the conversion efficiency from mass-energy to jet power would have to be an implausible 30% for the the radio source to be powered by Bondi accretion alone. Simulations from Gaspari et al. (2013) and Gaspari et al. (2015) showed that the transition between Bondi and chaotic cold accretion could boost the jet power by up to 100 times and occurs when $t_{cool}/t_{ff} \approx 10$. To see whether NGC4261 was a unique system and probe this transition by expanding the sample of similar galaxies, we found a Chandra archival sample of twelve additional early-type galaxies with powerful radio sources. We present a detailed analysis of the thermodynamic properties as well as t_{cool}/t_{ff} for this sample.

The structure of our paper is as follows. In Section 2, we describe our sample selection and data analysis. In Section 3, we present our measurements of the thermodynamic properties, the effect of metallicity on those measurements, t_{cool}/t_{ff} profiles, and comparison to simulations. In Section 5, we discuss how our sample adds new knowledge to the paradigm of precipitation-driven feedback in massive galaxies. We assume a lambda cold dark matter cosmology with $H_0 = 70$ km s^{-1} Mpc^{-1} and $\Omega_M = 0.3$ ($\Omega_\Lambda = 0.7$) throughout.

2. SAMPLE SELECTION AND DATA ANALYSIS

2.1. *Sample Selection*

In Voit et al. (2015a), NGC4261 exhibited an abnormally low central entropy as well as a t_{cool}/t_{ff} ratio less than 10. Because NGC4261 also has a powerful radio source (radio luminosity of 3×10^{40}erg s^{-1}), it appears to be undergoing a strong feedback outburst powered by chaotic cold accretion fed by the precipitation of cold clouds out of the hot atmosphere (Voit et al. 2015a). To determine if NGC4261 is a unique system, we chose a sample of nearby ($z < 0.02$) giant early type galaxies hosting radio sources with power greater than 10^{23} W Hz^{-1} at 1.4 GHz (see Table 2.1). Other samples can include some of our galaxies, but our sample was selected with emphasis on the presence of powerful radio sources because we wanted to probe galaxies most similar to NGC4261.

Of particular interest are NGC4374 (M84), NGC1316 (Fornax A), and IC 4296 because they had the best data quality of the sample. Each source represents a different manifestation of a powerful radio source. M84 is host to an FRI radio jet and exhibits OVI emission Finoguenov & Jones (2001). Fornax A has a weak core in the radio (250 mJy), but its radio lobes are some of the brightest radio sources in the sky (125,000 mJy) (Ekers et al. 1983). IC4296 is the BCG in a nearby galaxy group (Abell 3565), and HST spectroscopy indicates a central black hole mass of $\sim 10^9 M_\odot$ Dalla Bontà et al. (2009). Recent VLA D-configuration observations reveal 160 kpc diameter radio lobes, located over 230 kpc from the AGN host galaxy (Grossova et al. 2019).

2.2. *Chandra data reduction*

We reprocessed the archival *Chandra* data listed in 2.1 using CIAO 4.9 and CALDB 4.7.4. The data were cleaned to remove time intervals with anomalously high background by applying the "*deflare*" script in CIAO. Bright point sources were identified and removed using the "*wavdetect*" script. In some cases, there were significant point sources in the centers of the galaxies. These were not removed in the CIAO data cleaning process. We opted to incorporate the effect of point sources in the spatially-resolved spectral analysis step.

2.3. *Spectral Analysis*

In our spectral analysis, we obtained deprojected radial profiles of thermodynamic quantities. To prepare the spectra, we defined radial annuli each containing at least 300 counts. At temperatures around $0.7 - 1$ keV, very few counts are required for a robust X-ray temperature estimate. The images were background subtracted prior to fitting using background regions from each science image.

We obtained the profiles using `XSPEC` v. 12.9 (Arnaud 1996) using the `projct` model. We restricted the energy range for the spectral fitting to $0.6 - 2.0$ keV. In some cases, we held the temperature constant across multiple

Table 1
Chandra Observations of Giant Ellipticals

Name	z	D (Mpc)	Scale (arcsec kpc^{-1})	N_H ($10^{20} cm^{-2}$)	1.4 GHz (W Hz^{-1})	OBSID	Exposure (ks)	Net Counts per bin	Profile Made (Y/N)	Entropy Slope (1-10 kpc)
NGC4261	0.007	31.32	0.152	1.58	2.29×10^{24}	9569	100.34	1600	Y	1.09±0.07
IC4296	0.012	50.64	0.246	4.09	5.52×10^{24}	3394	24.84	800	Y	1.12±0.12
NGC1316	0.006	25.51	0.124	2.13	1.99×10^{22}	2022	29.86	450	Y	0.80±0.08
NGC4374	0.003	12.80	0.062	2.78	1.25×10^{23}	803	28.46	650	Y	0.75±0.05
IC1459	0.006	25.51	0.124	1.17	9.97×10^{22}	2196	58.00	300	Y	
NGC4782	0.015	63.08	0.306	3.58	3.33×10^{24}	3220	49.33	320	Y	
NGC5419	0.014	58.94	0.286	5.55	1.46×10^{23}	5000	14.81	320	Y	
NGC7626	0.011	46.48	0.225	5.05	2.22×10^{23}	2074	26.54	370	Y	
NGC193	0.015	63.08	0.306	2.79	4.68×10^{23}	11389	93.13	300	N	
NGC315	0.016	67.20	0.326	5.92	9.73×10^{23}	4156	53.84	930	N	
NGC741	0.018	75.42	0.037	4.44	3.27×10^{23}	17198	91.02	1500	Y	
NGC3801	0.011	46.48	0.225	2.18	2.96×10^{23}	6843	59.20	330	N	
NGC3894	0.011	46.48	0.225	1.71	1.25×10^{23}	10389	38.54	300	N	

annuli but allowed the densities for each shell to be independently estimated (see Appendix A).

NGC193, NGC3801, and NGC3894 were removed from the set of profiles because they had counts insufficient to obtain a deprojected temperature profile. NGC4782 had sufficient counts to extract a profile but had bright central point sources resulting in large uncertainties in the central bins. For NGC1316 and IC4296, we did not include the central spectral bin.

2.4. *Thermodynamic Properties*

2.4.1. *Electron Density Profiles*

To determine the electron density, we use the normalization calculated from the deprojected profile. The normalization in the `projct` model is proportional to the total emission measure within the extraction volume (Equation 1), where D is the angular diameter distance in cm, n_e and n_p are the electron and proton densities, respectively, in cm^{-3}, and V is the volume of the emission region in cm^3.

$$\eta = \frac{10^{-14}}{4\pi D^2} \int n_e n_p dV \tag{1}$$

Solving Equation 1 for n_e (Equation 2) in each spectral bin gives us the deprojected electron density profile.

$$n_e(r) = \sqrt{\frac{4\pi\eta(r)D^2}{10^{-14}(n_e/n_p)V(r)}} \tag{2}$$

2.4.2. *Entropy and t_{cool}/t_{ff} Profiles*

The gas entropy profile in terms of X-ray observables is $K = kT_X(r)n_e(r)^{-2/3}$. To compute the entropy profile, the electron density and temperature must have the same bin size. To achieve this, we assumed a constant temperature across the density profile bins included in each temperature bin because the variations in temperature within the profile are small.

The free-fall time is $t_{ff} = (2r/g)^{1/2}$ and the free-fall time is $tc = \frac{3}{2}\frac{nkT}{n_e n_H \Lambda}$, where n is the total number density of particles, n_e is the electron density, n_H is the hydrogen density ($n_e/1.2$), and Λ is the cooling function (Schure et al. 2009).

3. DISCUSSION

3.1. *Entropy Profiles*

In Figure 1, we show the entropy profiles for the candidates we were able to compute profiles for. While the resolution of the data were not sufficient to probe the inner $\sim$ 0.5 kpc for all early type galaxies except for NGC4261, we do see that the entropy profiles appear to more closely follow a single power law than a power law with a core excess.

A larger sample of giant elliptical galaxies from Lakhchaura et al. (2018) also reports entropy profiles for eight of our targets (NGC315, NGC741, NGC1316, NGC4261, NGC4374, NGC4782, IC4296, and NGC5419). While our bin sizes and radial ranges have small variations, our results are consistent within uncertainties though the studies were completed independently.

3.2. *Comparison of tc/tff to precipitation model*

Figure 2 shows the t_{cool}/t_{ff} for the galaxies with the best data resolution entropy profiles calculated. Of particular interest are the profiles of IC4296 and NGC4374 where the data are not of the resolution of NGC4261, but they still allow us to probe near the core.

Voit et al. (2015a) showed that t_{cool}/t_{ff} in the center of both single-phase and multi-phase galaxies remain above the expected threshold of $t_{cool}/t_{ff} \sim 10$. Further out from the center (1-10 kpc), galaxies with multi-phase gas have t_{cool}/t_{ff} that approximately tracks the threshold whereas galaxies with single-phase gas remain above the precipitation zone of $t_{cool}/t_{ff} \sim 5 - 20$ (blue shaded region in Figure 2). In their sample, they found that, unlike the rest of the sample, NGC4261 went below the $t_{cool}/t_{ff} \sim 10$ threshold in the center.

In our sample, the t_{cool}/t_{ff} profiles of NGC4374 and NGC1316 appear to match that of the single-phase galaxies from Voit et al. (2015a), where the ratio stays above the expected threshold of $t_{cool}/t_{ff} \sim 10$ across the radial profile. In contrast, IC4296 has a t_{cool}/t_{ff} profile that does go below the threshold in the center as we see in NGC4261. Multi-phase galaxies have $t_{cool}/t_{ff} > 10$ in the center, but can have $t_{cool}/t_{ff} < 10$ outside the central $\sim$kpc (Voit et al. 2015a).

The Hα emission in NGC4261 is nuclear rather than extended which is consistent with the picture of giant galaxies with single-phase gas having close to power law entropy slopes. Of our highlighted galaxies, IC4296 most closely resembles NGC4261 and with narrow band images from the Hubble and SOAR telescopes Grossova et al. (2019), we see that IC4296 also has only nuclear Hα emission.

3.3. *Metallicity Analysis*

Because the abundances of early type galaxies are difficult to accurately fit, we also explored the effect of assuming different abundances on the inferred profiles. In Figure 3, we show a comparison of the entropy profiles for NGC4261 for abundances of $0.3Z_\odot$,$0.5Z_\odot$, and $1.0Z_\odot$. The difference in assumed abundance causes an increase in the amplitude of the entropy as assumed abundance increases, but the slope of the entropy profile changes little. Assuming that the gas in the galaxy is well mixed, then we have shown that a change in abundance would cause a change in amplitude of the inferred entropy profile.

In comparing our results with entropy profiles from previous work, we find that different estimations for abundance result in small differences in the entropy profiles. However, when the same abundance profile is used, the results match. For the giant ellipticals examined by (Werner et al. 2012), the assumed abundances in the central kpc were generally around $Z \sim 0.5Z_\odot$, but $Z \sim 0.3Z_\odot$ and $Z \sim 1.0Z_\odot$ are also typically used for abundance estimations in giant ellipticals (Werner et al. 2012), (Wang et al. 2019), (Li & Bryan 2014b).

The slope of the relations between abundance and electron density for NGC1316, NGC4261, NGC4374, and IC4296 are -0.43 ± 0.04, -0.43 ± 0.04, -0.39 ± 0.11, and -0.29 ± 0.18, respectively. The relationship between electron density and abundance is inversely linear, with higher abundances resulting in a lower electron density

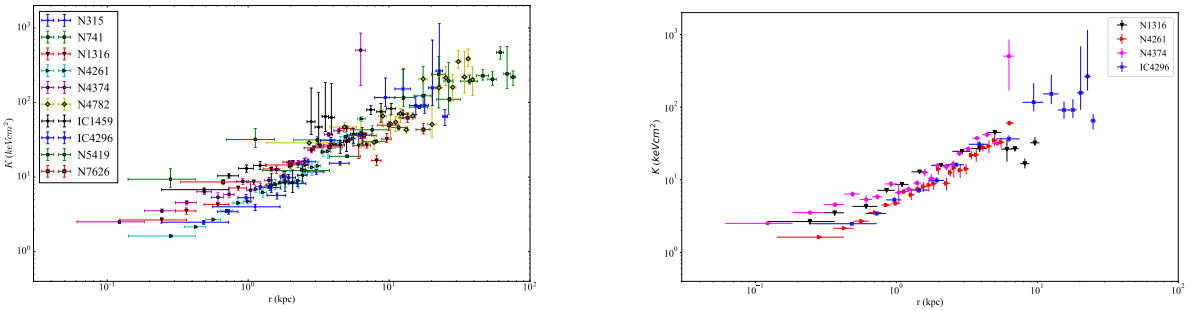

Figure 1. On the left, we show entropy profiles for our sample of early type galaxies. Not included are NGC193, NGC3894, and NGC3801 because they had insufficient counts to make a profile. On the right, we highlight the entropy profiles of our galaxies with best data quality (NGC4261, IC4296, NGC1316, NGC4374). On the right, we can see that the entropy profile of IC4296 closely resembles NGC4261 while the profiles of NGC1316 and NGC4374 do not.

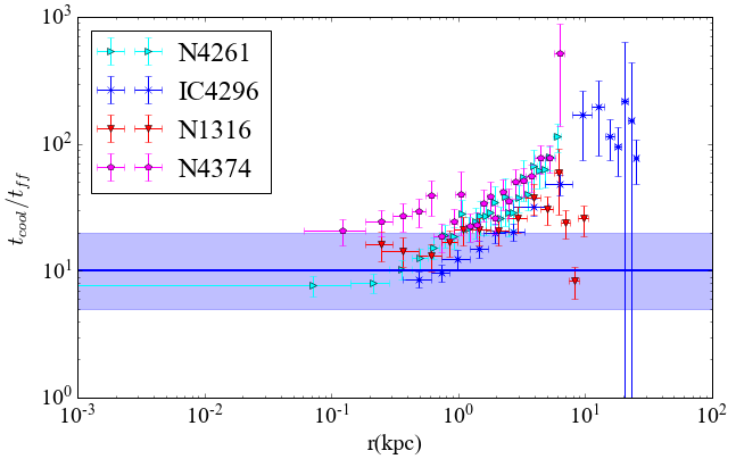

Figure 2. t_c/t_{ff} profiles for the galaxies with the best S/N. The blue shaded region ($t_c/t_{ff} = 5-20$) represents the precipitation limit where multi-phase gas is found for $r = 1-10$kpc. We find that like NGC4261, IC4296 dips below the threshold of $t_c/t_{ff} \approx 10$ in the center while the other galaxies do not.

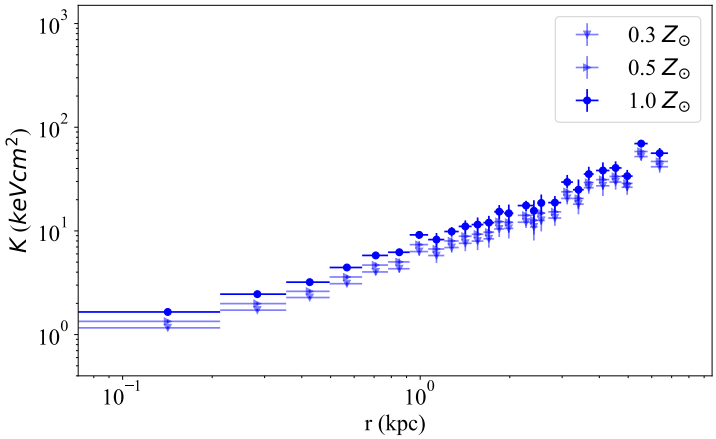

Figure 3. Here we show a comparison of the entropy profiles for NGC4261 for different values of abundance. The lines represent (from top to bottom), 1.0 $Z_\odot$ (blue circles), 0.5 $Z_\odot$ (blue right-facing triangles), and 0.3 $Z_\odot$ (blue downward-facing triangles). For increasing values of metallicity, the amplitude of the entropy profile increases. Therefore, if a galaxy is more metal-rich in the center than we have assumed, the cores could be somewhat flatter than we have found.

measurement. Using the estimated slope of the relation, we can estimate the change in electron density for different values of abundance. If the inferred temperature is independent of the assumed abundance, then $n_e \propto 1/Z$ so $K \propto Z^{2/3}$.

If the abundance is actually higher in the center, then assuming a constant metallicity profile means that the the metallicity is underestimated in the center and density is overestimated, and thus, the central entropy would be underestimated. If a galaxy's gas is more metal-rich in the center than we have assumed, the cores could have somewhat flatter cores than shown in our entropy profiles.

3.4. *Comparison to Simulations*

Voit et al. (2015b) showed that the slope of the entropy profiles correlates with the presence of multiphase gas outside of the central kpc of an early-type galaxy. Galaxies with an entropy slope of $\sim r^{2/3}$ have multiphase gas present for $r > 1$ kpc, and galaxies with an entropy slope of $\sim r$ have only single-phase gas. Figure 4 shows a comparison between our data for NGC4261 and simulations from Wang et al. (2019) for both single-phase and multi-phase gas elliptical galaxies. The initial conditions for the simulations are modeled after early-type galaxy data with the multi-phase initial conditions from NGC5044 and the single-phase initial conditions from NGC4472. The current simulations only resolve to a radius of 1 kpc, so our data reaches closer to the core than the simulations. However, we can still draw comparisons in the 1-10 kpc range.

From Makarov et al. (2014), the velocity dispersions of NGC5044 and NGC4472 are 224.9 ± 9.1 kms^{-1} and 282 ± 2.9 kms^{-1}, respectively, while the velocity dispersion for IC4296 and NGC4261 are 327.4 ± 5.4 kms^{-1} and 296.7 ± 4.3 kms^{-1}, respectively. Because velocity dispersion correlates with the entropy profile slope (Voit et al. 2015a) and the velocity dispersions of the simulated galaxies differ from NGC4261 and IC4296, we do not necessarily expect the simulated profiles to be exact matches to our data.

Each line represents a 150 Myr time step. The simulations do not resolve the cores of the galaxies, but we can still compare the slopes between $1 - 10$ kpc. The simulated entropy profiles from (Wang et al. 2019) match the results of (Voit et al. 2015b), where multi-phase galaxies follow an entropy slope of $K(r) = 3.5 r_{kpc}^{2/3}$keV cm^2, representing the threshold of $t_c/t_{ff} \approx 10$, and single-phase galaxies follow an entropy slope of $K(r) = 5 r_{kpc}$keV cm^2, representing an outflow solution. The implication of these combined works is that self-regulated AGN feedback can maintain the stability of the single-phase or multi-phase gas.

When we compare the data from our sample, specifically IC4296 and NGC4261 to the simulation, we see that the the multi-phase gas simulation does not match the data well. Based on the entropy profile slopes of our data, we did not expect them to be consistent. When we compare our data to the single-phase simulation, it does appear to regulate to approximately the same entropy slope as our data. For some time steps, the center of the entropy profile simulation does flatten out which may indicate periods of lower AGN activity.

4. CONCLUSIONS

While the resolution and quality of the archival data available reduced our sample size, we were able to obtain deprojected temperature and density profiles as well as entropy and cooling time profiles for nine additional elliptical galaxies. Of particular interest in our sample were the two ellipticals with the best signal-to-noise, IC4296 and NGC1316. The entropy profiles appeared to follow a $r^{2/3}$ power law as discussed in Voit et al. (2015a). However, the most striking result comes from the t_{cool}/t_{ff} profiles. We find that the profile for NGC1316 behaves like many other known early type galaxies with the t_{cool}/t_{ff} ratio remaining above the threshold of $t_{cool}/t_{ff} \approx 10$. However, IC4296, like NGC4261 has a t_{cool}/t_{ff} ratio that dips below the threshold. It appears that NGC4261 is not a unique system and NGC4261 and IC4296 may represent a transitional stage of AGN feedback.

This work was supported by a *Chandra* archive grant. Acknowledgements here

REFERENCES

Arnaud, K. A. 1996, in Astronomical Society of the Pacific Conference Series, Vol. 101, Astronomical Data Analysis Software and Systems V, ed. G. H. Jacoby & J. Barnes, 17
Dalla Bontà, E., Ferrarese, L., Corsini, E. M., et al. 2009, ApJ, 690, 537
Ekers, R. D., Goss, W. M., Wellington, K. J., et al. 1983, A&A, 127, 361
Finoguenov, A., & Jones, C. 2001, ApJ, 547, L107
Gaspari, M., Brighenti, F., & Temi, P. 2015, A&A, 579, A62
Gaspari, M., Ruszkowski, M., & Oh, S. P. 2013, MNRAS, 432, 3401
Gaspari, M., Ruszkowski, M., & Sharma, P. 2012, ApJ, 746, 94
Grossova, R., Werner, N., Rajpurohit, K., et al. 2019, arXiv e-prints, arXiv:1903.03198
Lakhchaura, K., Werner, N., Sun, M., et al. 2018, MNRAS, 481, 4472
Li, Y., & Bryan, G. L. 2014a, ApJ, 789, 54
—. 2014b, ApJ, 789, 153
Makarov, D., Prugniel, P., Terekhova, N., Courtois, H., & Vauglin, I. 2014, A&A, 570, A13
McCourt, M., Sharma, P., Quataert, E., & Parrish, I. J. 2012, MNRAS, 419, 3319
McNamara, B. R., & Nulsen, P. E. J. 2007, ARA&A, 45, 117
—. 2012, New Journal of Physics, 14, 055023
Pizzolato, F., & Soker, N. 2005, ApJ, 632, 821
—. 2010, MNRAS, 408, 961
Schure, K. M., Kosenko, D., Kaastra, J. S., Keppens, R., & Vink, J. 2009, A&A, 508, 751
Sharma, P., McCourt, M., Quataert, E., & Parrish, I. J. 2012, MNRAS, 420, 3174
Voit, G. M., Bryan, G. L., O'Shea, B. W., & Donahue, M. 2015a, ApJL, 808, L30
Voit, G. M., & Donahue, M. 2015, ApJ, 799, L1
Voit, G. M., Donahue, M., O'Shea, B. W., et al. 2015b, ApJ, 803, L21
Wang, C., Li, Y., & Ruszkowski, M. 2019, MNRAS, 482, 3576
Werner, N., Allen, S. W., & Simionescu, A. 2012, MNRAS, 425, 2731

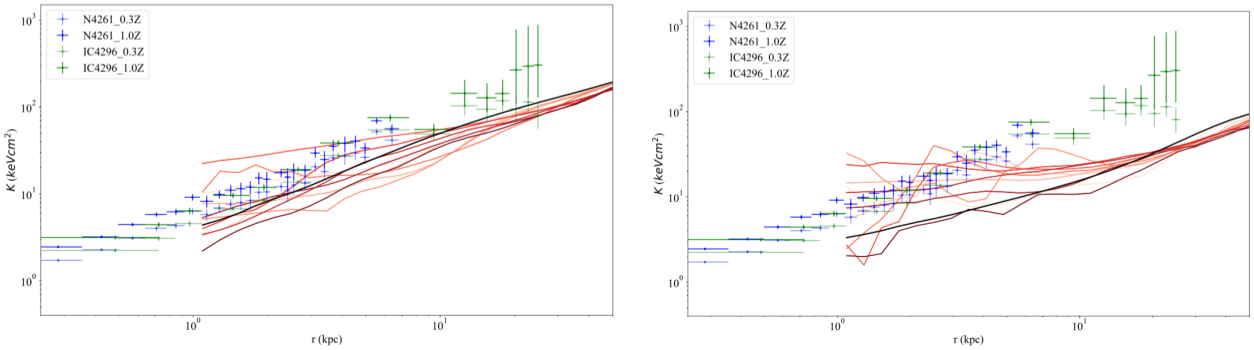

Figure 4. These two plots compare our entropy profiles of NGC4261 and IC4296 to simulations of giant elliptical galaxies with single-phase gas (left) and multi-phase gas (right) Wang et al. (2019). The simulations are in red and represent profiles plotted every 150 Myr going from dark red to light red. The initial conditions are given by the black line. The data for NGC4261 are in blue and the data for IC4296 are in green. The lighter shade data points represent the range of entropy for variation in metallicity. Initial conditions for the single-phase gas simulations came from NGC4472 and initial conditions for the multi-phase gas simulations came from NGC5044. Our data are largely consistent with the single-phase gas simulation which we expected, given the absence of extended multi-phase gas and the slope of the entropy profile.

APPENDIX

APPENDIX

Table 2 Radial profile properties for each galaxy with significant counts to obtain a deprojected temperature and density profile. Errors given for radius are the bins widths, and errors given for density and temperature are 90% confidence intervals calculated by `XSPEC`.

Name	**Radius** (kpc)	$\boldsymbol{\sigma_r}$ (kpc)	**kT** (keV)	$\boldsymbol{\sigma_{kT-}}$ (keV)	$\boldsymbol{\sigma_{kT+}}$ (keV)	$\mathbf{n_e}$ (cm^{-3})	$\boldsymbol{\sigma_{n_e-}}$ (cm^{-3})	$\boldsymbol{\sigma_{n_e+}}$ (cm^{-3})	**K** ($keVcm^{-2}$)	$\boldsymbol{\sigma_{K-}}$ ($keVcm^{-2}$)	$\boldsymbol{\sigma_{K+}}$ ($keVcm^{-2}$)
N4261	0.071	0.035	0.719	0.016	0.016	0.575	0.029	0.029	1.04	0.042	0.042
N4261	0.213	0.071	0.719	0.016	0.016	0.27	0.009	0.009	1.721	0.054	0.054
N4261	0.354	0.071	0.719	0.016	0.016	0.168	0.007	0.007	2.363	0.088	0.088
N4261	0.496	0.071	0.753	0.025	0.024	0.108	0.006	0.006	3.327	0.161	0.162
N4261	0.638	0.071	0.753	0.025	0.024	0.071	0.005	0.005	4.402	0.259	0.259
N4261	0.78	0.071	0.753	0.025	0.024	0.063	0.007	0.007	4.769	0.379	0.38
N4261	0.922	0.071	0.763	0.042	0.042	0.036	0.003	0.003	7.05	0.6	0.602
N4261	1.063	0.071	0.763	0.042	0.042	0.041	0.009	0.009	6.429	1.001	1.004
N4261	1.205	0.071	0.763	0.042	0.042	0.031	0.004	0.004	7.73	0.813	0.813
N4261	1.347	0.071	0.74	0.08	0.061	0.025	0.005	0.005	8.6	1.255	1.388
N4261	1.489	0.071	0.74	0.08	0.061	0.023	0.005	0.005	9.027	1.535	1.654
N4261	1.631	0.071	0.74	0.08	0.061	0.022	0.005	0.005	9.475	1.561	1.69